Applied Surface Science 666 (2024) 160349

Contents lists available at ScienceDirect

Applied Surface Science

journal homepage: www.elsevier.com/locate/apsusc

Full length article

Near-surface analysis of magnetron sputtered AlCrNbYZrN$_x$ high entropy materials resolved by HAXPES

Aishwarya Srinath [a], Kristina von Fieandt [a], Stefan Fritze [a], Leif Nyholm [a], Erik Lewin [a], Rebecka Lindblad [a,b,*]

[a] Department of Chemistry – Ångström Laboratory, Uppsala University, Box 538, SE – 751 21 Uppsala, Sweden
[b] Department of Physics and Astronomy, Uppsala University, Box 516, SE – 751 20 Uppsala, Sweden

ARTICLE INFO

Keywords:
Multicomponent alloys
Passivation
Corrosion
Metal nitrides
Synchrotron radiation

ABSTRACT

Hard X-ray photoelectron spectroscopy (HAXPES) was used to perform a non-destructive depth profile of AlCrNbYZrN$_x$ (x = 0 to ~50 at.%) thin films. The outermost native oxide of the pristine thin films contained the highest coordination oxides of every metal. Substoichiometric oxides or oxynitrides were found underneath. After exposure to 1.0 M HCl, increases in the most highly coordinated oxides of Cr, Nb, and Al in films with up to 37 at.% N were observed, suggesting that the low coordination oxides and oxynitrides in the subsurface had been further oxidised and were intermediary compounds in the passivation process. Al and Y oxides were lost to the HCl electrolyte, in agreement with their respective Pourbaix diagrams. The film with 49 at.% N showed little to no change in the data due to its high porosity which led to the oxide being detected at all probed depths. The metal core level spectra revealed a preferential order in which nitrogen bonded with the different metals. Nitrogen interacted first with Y, then Zr, then Al and Nb, and lastly Cr as the nitrogen content was increased.

1. Introduction

High entropy alloys, also known as multicomponent alloys, consist of four or more metals in major amounts. Intimate knowledge of their surface oxidation and speciation processes is key to developing highly corrosion resistant high entropy alloys. Due to the large number of metals present in major amounts [1–4], many different metal oxides may be found on the surface of a high entropy material. In a conventional alloy, the corrosion rate is largely determined by the thermodynamic and kinetic stability of its major metal. This restricts the utility of the alloy to the stability window of one metal. High entropy alloying strategies could significantly broaden the range of conditions in which an alloy is used. When oxides of the more noble metals in an alloy populate the surface to form an impervious layer, the underlying composition of the bulk alloy becomes less critical, and less noble elements can also be used. With sound alloying choices, coatings of high entropy alloys could deliver extensive protection due to the wider degree of passivity arising from the enrichment and spontaneous regeneration of the many different oxides on the surface.

However, when studying high entropy materials, something as routine as profiling the passive layer presents a significant challenge. Transition metals may form several compounds with different oxidation states depending on their exposure to oxygen. In a high entropy alloy, the number of different species increases quickly. As the passive layer is only a few nanometres thick, the distribution of the different oxides is challenging to discern even with the most highly resolved techniques [5–10].

Synchrotron-based hard X-ray photoelectron spectroscopy (HAXPES) permits the study of both the bulk material and native oxide without having to remove any surface material [11,12]. Sputtering, which is often conducted with laboratory XPS machines, preferentially removes lighter elements such as nitrogen and oxygen and can produce unwanted artefacts in materials containing both heavy and light elements, such as a metal nitride or oxide [13]. The conflation of these artefacts with the actual data may then give a distorted understanding of the properties of a material. The multiple photon energies available at a synchrotron radiation source make it possible to conduct a non-destructive depth profile of the studied material. This is particularly useful for the study of high entropy nitrides [14,15].

Corrosion and passivation in a high entropy alloy is comprised of many simultaneous oxidation and dissolution reactions. To identify the intermediate stages contributing to the formation of a stable passive layer, both the passive layer and the region directly beneath it must be probed, in order to map the pathways to the formation of a mature native oxide. The stability of the surface oxide in any given environment, and thus the corrosion resistance of the alloy, is determined

* Corresponding author at: Department of Physics and Astronomy, Uppsala University, Box 516, SE – 751 20 Uppsala, Sweden.
E-mail address: rebecka.lindblad@physics.uu.se (R. Lindblad).

https://doi.org/10.1016/j.apsusc.2024.160349
Received 7 December 2023; Received in revised form 23 April 2024; Accepted 19 May 2024
Available online 23 May 2024

by the electron transfer kinetics and thermodynamic stabilities of the individual oxides, the microstructures of the material, and its elemental composition [16–19].

High-entropy alloys can be synthesised as bulk materials using e.g., arc-melting, or as thin films using e.g., sputter deposition where the latter is well-suited for producing high-entropy nitrides. For high entropy nitride coatings, a large focus has been on their mechanical properties, but a few studies of oxidation in air or in aqueous solutions have also been reported, see Ref. [20] and references therein. The focus of the present work is the $AlCrNbYZrN_x$ alloy system, produced as thin films using reactive DC magnetron sputtering. The microstructural and mechanical properties of such thin films were previously studied by von Fieandt et al. by combining X-ray diffraction, scanning electron microscopy and mechanical testing [21,22]. It was found that denser and harder films with high N content were obtained by increasing both the temperature and substrate bias. Srinath et al. [23] probed the corrosion resistances of sputter-deposited $AlCrNbYZrN_x$ thin films using electrochemical techniques. Nyquist plots from impedance measurements showed that $AlCrNbYZrN_x$ films with N contents between 13 and 50 at.% were able to withstand more than 72 h under immersion in 1.0 M HCl. Only the purely metallic film dissolved instantly, while the nitrogen-containing films underwent varying levels of pitting or homogeneous corrosion, with the densest films having the highest corrosion resistances after 72 h, establishing a clear link between microstructure (porosity) and corrosion resistance.

Here, we expand upon this by studying the passive layer in more detail before and after potentiodynamic polarisation to anodic potentials, which provides a driving force for surface oxidation and is the condition found in *e.g.,* electrochemical devices. We use HAXPES to show that the passivation of an alloy involves the step-wise oxidation of the different component metals. In an $AlCrNbYZrN_x$ multicomponent material, the different metals are expected to contribute to a compositionally complex surface with each of the metals forming several oxides, oxynitrides, hydroxides, and metal nitrides with different oxidation states [24–35]. This study details an extensive spectroscopic investigation into the near-surface environments of the $AlCrNbYZrN_x$ multicomponent system, including the naturally formed as well as the corroded passive layer. The metal-nitrogen interaction and its effects on the passive layer were also studied.

2. Methods

The samples consisted of thin films and the thin film deposition procedure and bulk composition analysis summarised below was reproduced from Refs. [21–23]. The films were deposited using a sputter system with an ultra-high vacuum chamber (Qprep500i from Mantis Deposition Ltd.) with a base pressure of $3.7 \cdot 10^{-10}$ Torr ($4.9 \cdot 10^{-8}$ Pa) at room temperature and $9 \cdot 10^{-7}$ Torr ($1.2 \cdot 10^{-4}$ Pa) during deposition at 500 °C. Three magnetrons were used: segmented Al/Cr (1:1), segmented Nb/Zr (1:1), and a Y target. The substrates used were α-$Al_2O_3(001)$ which after cleaning in acetone, were preheated at 500 °C for at least one hour to avoid the formation of temperature gradients. A rotating substrate holder ensured homogeneous composition of the resulting films. A substrate rf bias of −50 V was used for all depositions. The target powers were constant for all depositions and set to 130 W for Al/Cr, 250 W for Nb/Zr and 50 W for Y. The gas mixture consisted of Ar and N_2 (99.9999% and 99.9995% purity, respectively). The Ar and N_2 flows rates were adjusted in order to achieve different N_2 flow rate ratios ($R_N = N_2/(N_2+Ar)$), between 0 and 60%, resulting in the bulk compositions according to Table 1. The table is adapted from Srinath et al. [23] with the identical deposition procedure being used to fabricate the films. See Supplementary Information for details about the determination of the bulk composition, phase content and microstructure presented in Table 1.

The top surface morphology of the as-deposited films was studied by atomic force microscopy. A Bruker Dimension Icon ICON4-SYS instrument in AFM mode was used to carry out the measurements, with a high resolution scanasyst air tip in non-contact mode. An area of 500 x 500 nm^2 was mapped at a scan rate of 1 Hz.

Table 1
Bulk composition (determined by laboratory XPS and ERDA) of as-deposited $AlCrNbYZrN_x$ films in at.% (estimated uncertainty ±1 at.%-units) together with the structure (determined by XRD) and microstructure (determined by SEM). The data is adapted from Ref. [23] as the same thin film deposition procedure was used.

Al	Cr	Nb	Y	Zr	N	O	Phase composition	Microstructure
9	22	35	8	21	0	5	intermetallic phases	granular
8	22	29	7	18	13	3	nanocomposite*	fine-grained
7	19	25	7	18	23	1	nanocomposite*	dense fine-grained
5	13	22	7	16	37	0	nanocomposite*	dense columnar
5	12	18	3	13	49	0	NaCl-type nitride	columnar

* Nanocomposite consists of intermetallic phases and a NaCl-type nitride.

The thin films were corroded by exposing the samples to the electrolyte (1.0 M HCl) for two hours under open circuit potential (OCP) conditions followed by a polarisation from −0.7 V to +0.6 V vs. Ag/AgCl (3 M KCl) at a scan rate of 1 mV/s. The end value of 0.6 V was chosen to ensure the presence of an intact passive layer.

The HAXPES measurements were performed at beamline I09 at the Diamond Light Source [36]. This beamline is equipped with a Si(111) double crystal monochromator and a secondary monochromator using Si(001) channel cut. The photon energies used to probe different depths of the samples were 2351 eV, 4000 eV and 5922 eV, henceforth referred to as 2 keV, 4 keV and 6 keV respectively. The channel cut was used for a photon energy of 6 keV, but not for 2 keV and 4 keV. The photon bandwidth was approximately 250 meV for 6 keV and slightly broader for 2 keV and 4 keV. Photoelectrons were detected with a VG Scienta EW4000 HAXPES electron analyser using a pass energy of 100 or 200 eV and a slit of 0.3 mm, giving a maximum spectrometer resolution of 150 meV. The step size was 100 meV for Al 1s and Cr 2p and 50 meV for all other core levels. Due to the high photon flux delivered by the beamline, care needed to be taken to not saturate the detector of the electron analyser. This was done by reducing the pass energy to 100 eV when needed, which was for all core levels when using photon energies of 2 keV and 4 keV, and for Cr 2p and Al 1s when using a photon energy of 6 keV. An estimation of the total experimental resolution is obtained from the Gaussian width (FWHM) of the Au $4f_{7/2}$ core level of a gold reference. Fitting this core level with a Voigt profile and a fixed Lorentian FWHM of 0.33 eV [37] (see further details of the curve fit procedure below) gives Gaussian FWHM of 0.40 eV, 0.50 eV and 0.28 eV for the selected photon energies of 2 keV, 4 keV and 6 keV respectively when measured with a pass energy of 100 eV. The electron take-off angle was 82° for measurements with a photon energy of 6 keV, (*i.e.*, close to normal emission), but lowered to 60° for 2 keV and 4 keV to reduce the number of electrons reaching the detector. The information depth was estimated as $3 * IMFP * sin(\theta)$, where IMFP is the inelastic mean free path and θ the take-off angle. The IMFP was calculated using the TPP-2M formula in the Quases software [38] assuming ZrN as the matrix material with a density of 7.09 g/cm^3, as it has a similar value to that of the studied multicomponent materials, see supplementary information and Table S1 for further details.

The samples were contacted by using conductive copper tape. Even though the thin film samples were conducting, they were deposited on a non-conducting substrate, which caused some charging issues. Charging was monitored by checking the core level peak positions as a function of varying X-ray intensity, and when necessary, the X-ray intensity was lowered to minimise charging. The binding energy scale was corrected by placing the valence band edge (corresponding to the Fermi edge) at 0 eV binding energy. In a few cases, mainly for 13 and 23 at.% N samples measured with a photon energy of 2 keV, this did not work due to the porous nature of the samples or an insufficient contacting of the sample. In these cases the metal component were shifted manually (~0.1–0.3 eV) to the corresponding metal component of the

0 at.% N sample. For easy comparison, the intensities are normalised to the most intense feature or, in some cases, the metal/nitride peak. Only relative intensities of different components of a certain core level as well as binding energy shifts of a certain core level are discussed. Binding energy shifts are given with an uncertainty of 0.1 eV if not stated otherwise.

Oxidation state analysis was done via peak fittings of the core level spectra using the Igor Pro software and the SPANCF macro package [39, 40] together with the strategy outlined below. The fitting was always done using the Shirley-type background provided by the macro and as few peaks as possible. Peak fittings of the core level peaks with lowest oxidation state (as for metal and nitride components) were made using asymmetric Doniach–Sunjic-profiles [41]. The contribution from higher oxidation states (as for oxides) were modelled by symmetric Voigt profiles. The intensity ratio of the spin–orbit components was fixed according to the theoretical value (1:2 for $p_{1/2}$:$p_{3/2}$ levels and 2:3 for $d_{3/2}$:$d_{5/2}$ levels). Lorentzian broadenings relates to the natural atomic level widths and for all core levels the Lorentzian FWHM was fixed to the recommended value given by Campbell et al. [37]. The most bulk sensitive measurements of the 0 at.% and 49 at.% samples were used as models for the metal and nitride components respectively and the obtained Gaussian broadening, asymmetry, and spin–orbit splitting for these metal/nitride components were applied when fitting the other core level spectra. In a similar manner, the pristine material acted as a model for the corroded samples regarding number of peaks, core level shifts, and Gaussian widths. Oxide contributions were allowed to have a broader Gaussian width than metal and nitride contributions, partly due to the more complex lineshape for some oxides (compare e.g. Cr metal and Cr oxide in Ref. [42]) but also to account for the complex nature of the oxide in the multicomponent system. If more than one oxide was present, these were given the same Gaussian width if possible. In most cases, four components have been used to conduct the curve fit for each element, denoted *a* (grey), *b* (blue), *c* (yellow) and *d* (red) in order of increasing binding energy.

3. Results and discussion

3.1. As-deposited $AlCrNbYZrN_x$ films

Figs. 1–5 show the data for the as-deposited $AlCrNbYZrN_x$ films. The left hand side of each figure shows the core level spectra collected for every $AlCrNbYZrN_x$ film using photon energies of 2, 4 and 6 keV. The elemental metal position (solid black line) and the metal nitride position (dotted line) are also demarcated and were obtained by curve fitting. The curve fits, shown in the centre of each figure, are shown for the 0, 37 and 49 at.% N samples measured with a photon energy of 6 keV. Dotted lines (bgr) show the modelled background and solid black lines (sum fit) shows the sum of all fitted peaks, including the background. The right hand side of Figs. 1–5 shows a bar chart representation of the different components (metal, metal in N environment, metal oxide) acquired from the curve fits.

Details from the curve fits such as core level shifts, Gaussian widths (FWHM), spin–orbit splittings, asymmetry parameters for Doniach–Sunjic line profiles [39–41], as well as the input value for the Lorentzian widths (FWHM) [37] are found in Table S3 in Supplementary Information. The curve fits of the data collected at a photon energy of 4 keV did not give any new information and hence were not discussed further. Representative overview spectra, as well as N 1s and O 1s core level spectra are shown in Figure S1–S3 in Supplementary Information. The discussion focuses on the metal core level spectra.

The studied as-deposited films were stored in ambient conditions and thus had their native oxide present. The different X-ray energies have been used to vary the depth sensitivity of the measurements and obtain information of the region between the bulk and the outermost surface. As the X-rays will invariably encounter the surface first, any collected spectrum will always contain some contribution from the surface regardless of the energy. Measurements conducted at a photon energy of 2 keV will show larger contributions from the surface compared to those conducted at 6 keV. A higher photon energy produces photoelectrons with higher kinetic energies and a longer inelastic mean free path, thus giving more bulk sensitive measurements [43,44].

With a photon energy of 6 keV, the estimated information depth is approximately 20 nm for all the core levels except Al 1s, which has a much higher binding energy compared to the others. Adjusting for this gives an estimated information depth of 17 nm for Al 1s, allowing exploration well into the bulk. This can be compared to the calculated information depth for the 2 keV measurements in this work, where Al 1s has an information depth of 4 nm, and the other core levels between 7–8 nm. See Table S2 in Supplementary Information for all calculated information depths.

Peaks with lower binding energies represent the components with lowest oxidation state, *i.e.*, the metallic and nitride-like components. The components with higher binding energies correspond to the oxides. A comparison of the surface (2 keV) and bulk (6 keV) sensitive measurements show that the oxide is indeed found on the surface and we note that all metals are found in the oxide.

The interpretation of the presented data comes with an important caveat. This mixed alloy system is likely containing mixed metal oxides. This suggestion is supported by the O 1s core level spectra, shown in Supplementary Information Figure S3, which mainly show one broad peak that cannot easily be separated into different metal oxides. The mixed nature of the oxide makes it challenging to determine the exact stoichiometries due to the sheer multiplicity of possible compounds. The elements will thus be described according to their oxidation state (e.g., Cr^{3+}) or chemical environment, and any assigned stoichiometries are tentative and were obtained through references to the literature and the Pourbaix diagram of the metal.

3.1.1. Al 1s

Fig. 1 (left) shows the peaks in the core level spectra shifting to higher binding energies from the elemental metal (solid black line) to the metal nitride (dotted line) with increasing N content.

The curve fits of the 0 at.% N sample measured with a photon energy of 6 keV showed a low-energy peak, *a*, with a Al 1s binding energy of 1557.9 ± 0.2 eV and an asymmetry towards higher binding energy, assigned to metallic Al [45]. Shifted 3.0 eV towards higher binding energy was a symmetric peak, assigned to an aluminium oxide. This shift is larger than the reported metal-oxide shift of an AlCrFe alloy [11], indicating a different type of oxide. The fits of the 13 and 23 at.% N films also showed the same peaks separated by 3.0 eV, suggesting that they, like the 0 at.% N film, consisted of metallic and oxidised Al, with no nitride-like contributions.

The 37 at.% N sample showed a broader peak at high binding energy than the 13 and 23 at.% N films, requiring a third component *b* for the fit. The new component *b*, with *b*-*a* core level shift of +2.4 eV, was associated with aluminium in a nitride-like environment and is shaded in blue. A notable increase in this component was observed in the 2 keV measurements (compared to 6 keV). This species was situated close to the outermost oxide due to its higher intensity in the surface sensitive measurements, and as it was not present in the films with lower N content, it is assumed to be an oxynitride. For the 49 at.% N sample, only components *b* and *c*, with a separation of 1.0 eV, were required, corresponding to aluminium in chemical environments similar to AlN and $Al_2 2O_3$ [24]. The data suggests that the nitrogen atoms did not interact with Al at N concentrations below 37 at.%.

3.1.2. Cr 2p

To the left in Fig. 2 we note an increase in the background on the high-binding energy side of the Cr 2p core level when measured with a photon energy of 2 keV and we assign this to Nb, Y and Zr LMM and LMN Auger lines (see Figure S1 in Supplementary Information). The 0–37 at.% N core level films required three components *a, c* and *d*

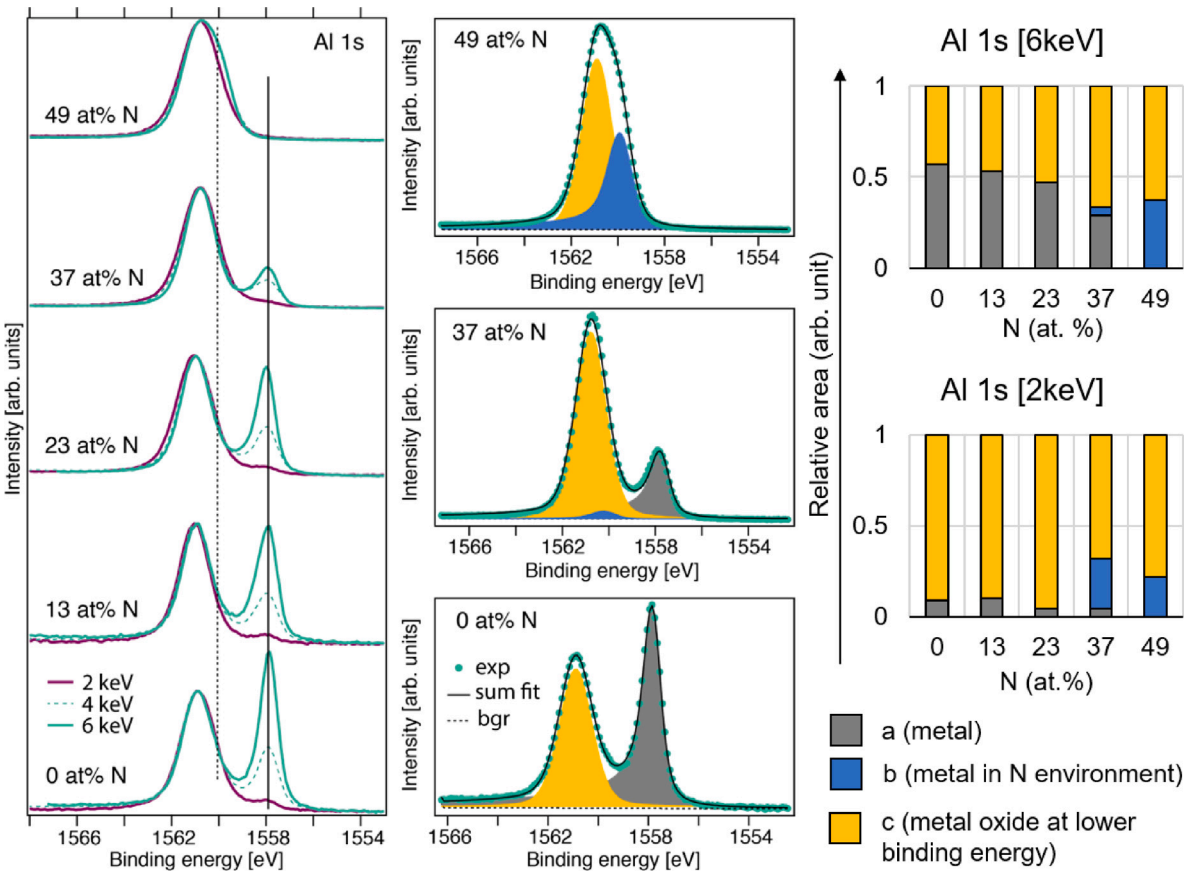

Fig. 1. Al 1s spectra collected using photon energies of 2, 4 and 6 keV. The left hand side shows the overlaid spectra for all as-deposited $AlCrNbYZrN_x$ samples at all energies, with the intensities normalised to the oxide component. Solid (dotted) vertical line indicate position of metal (nitride) components. The centre panel shows the curve fits of the 0, 37 and 49 at.% N samples measured with a photon energy of 6 keV. The shaded areas from the curve fits have been used to create the bar charts on the right where the metal is in grey, the nitride-like (or oxynitride) is in blue and the oxide is in yellow.

(all spin–orbit doublets) to fit the spectrum. The lowest binding energy component *a* with a Cr $2p_{3/2}$ binding energy of 573.4 ± 0.2 eV, assigned to metallic Cr, was modelled with an asymmetric lineshape, and was present in all the films below 49 at.% N. An additional component *c* with a *c-a* shift of +0.53 was also needed to complete the model of the lowest energy feature. Component *c*, with a *c–a* shift of +0.53 eV was seen for the 0–37 at.% N films, and was found to increase in the more surface sensitive measurements. It appeared to be independent of N content and hence may have been a low-coordinated oxide with a chemical environment similar to CrO [46]. The highest binding energy component *d*, with a *d-a* shift of approximately +3.0 eV was assigned to Cr^{3+} [47]. Its intensity was larger in the surface sensitive measurements relative to *a* and *c* in all the films, indicating that it was found on the outermost surface as an oxide. Component *d* also had a broad Gaussian width of 3.0 eV. Its large width could indicate a mixture of Cr oxides. Chemical shifts of +2.4 eV and +3.4 eV to metallic Cr have been reported for Cr_2O_3 and $Cr(OH)_3$ respectively [47]. A hydroxide is however not supported by the O 1s core level spectrum, see Supplementary Information Figure S3. The *d-a* shift was +3.1 eV in the 0 and 23 at.% N samples, but a slightly smaller shift of 2.8 (± 0.1) eV was observed for the 37 at.% N sample, potentially indicating another type of oxide. The spectrum of the 23 at.% N sample measured with a photon energy of 2 keV shows a shoulder around 582 eV, which is an error and is discussed further in Supplementary Information, Figure S4.

For the 49 at.% N film, there was no metallic *a* component. The Cr 2p core level spectra were modelled with three components: *b* for Cr in a nitride-like environment, *c* and *d* for Cr in oxide environments. Both *c* and *d* components increased in intensity towards the surface, supporting that these components resulted from oxidised chromium with oxide or oxynitride character. The *b-a* shift was +1 eV compared to the metallic component seen in the samples with lower nitrogen content, in agreement with earlier studies [48]. The core level shift of *c-b* and *d-b* was +1.2 eV and +1.6 (±0.15) eV respectively. We note that component *c* in the 49 at.% N film has a binding energy of 576.2 ± 0.2 eV, which overlaps with component *d* in the 37 at.% N sample, indicating a similar oxide. Component *d* in the 49 at.% N film is shifted even further in binding energy, indicating that this can be an oxynitride.

The Cr 2p spectra show that Cr was found in a metallic or oxide environment for the samples with 0, 13, 23 and 37 at.% N. No nitride-like Cr was detected in these samples. In the 49 at.% N sample, there was no metallic chromium and the chromium with lowest oxidation state was assigned to chromium in a nitride-like environment. Similar to Al, it appeared that the nitrogen in the film was not in the immediate vicinity of the Cr atoms unless the N:Cr concentration approached 1:1.

3.1.3. Nb 3d

The Nb 3d spectra of the 0 at.% and 13 at.% N samples measured with a photon energy of 6 keV showed two spin–orbit doublets, see Fig. 3. Component *a* with a Nb $3d_{5/2}$ binding energy of 202.2 ± 0.2 eV and an asymmetric line shape was assigned to metallic Nb. Shifted 5.3 ± 0.15 eV towards higher binding energy was a spin–orbit doublet with symmetric form, denoted *d*, whose shift was in good agreement with Nb^{5+} usually found in Nb_2O_5 based on Pourbaix diagrams and previous studies [46,49,50].

For the 23 at.% N sample, the *d-a* shift was 0.3 eV smaller than in the 0 and 13 at.% N samples, indicating the Nb atoms were affected

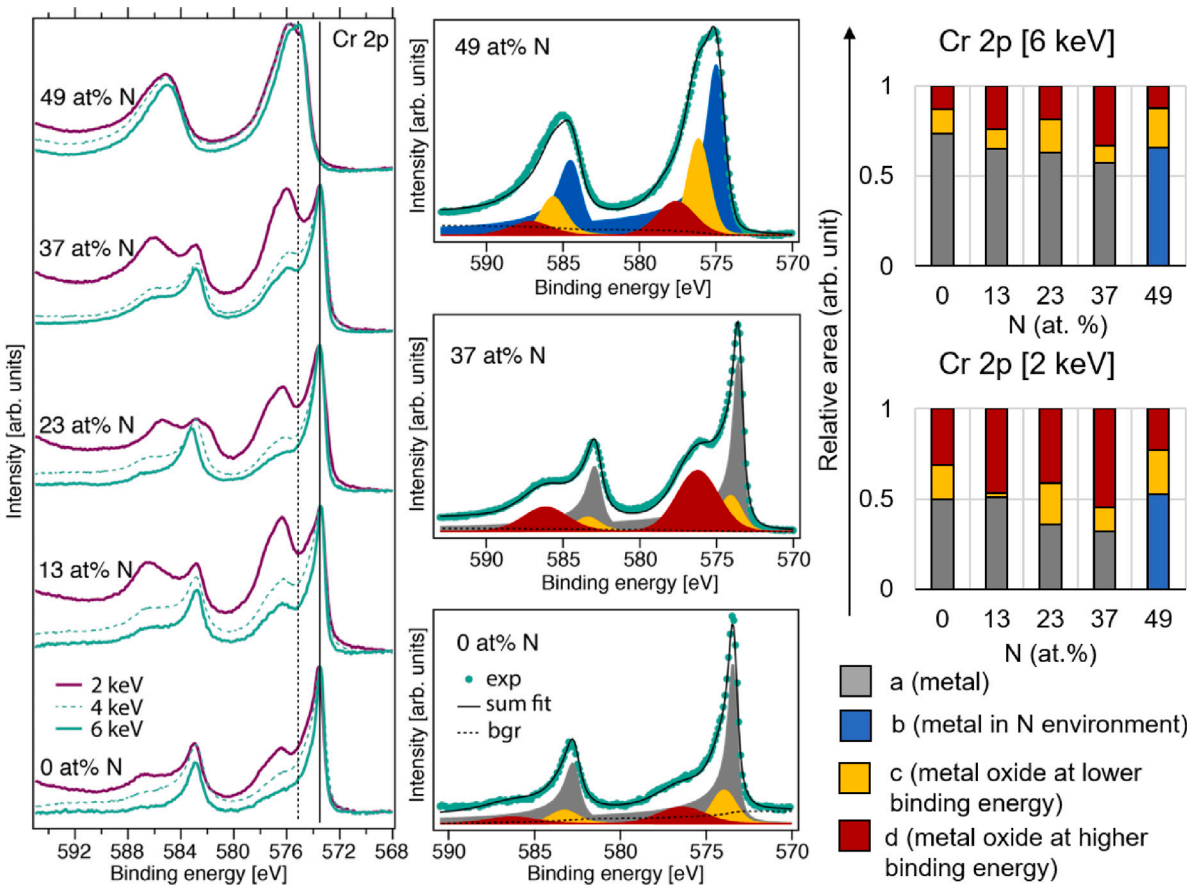

Fig. 2. Cr 2p spectra collected using photon energies of 2, 4 and 6 keV. The left hand side shows the overlaid spectra for all as-deposited $AlCrNbYZrN_x$ samples at all energies, with the intensities normalised to the highest peak. Solid (dotted) vertical line indicate position of metal (nitride) components. The centre panel shows the curve fits of the 0, 37 and 49 at.% N samples measured with a photon energy of 6 keV. The shaded areas from the Cr $2p_{3/2}$ curve fits have been used to create the bar charts on the right where the metal is in grey, the nitride-like is in blue and the oxides are in yellow and red (with a different assignment of the oxides for the 49 at.% N sample, see text for further details).

by the higher N concentration and that component *a* is no longer purely metallic-like. In the surface sensitive measurement at 2 keV of the 23 at.% N film, a third component *c* was also required to fit the spectrum, with a *c*-*a* shift of +3.8 eV. Based on Pourbaix diagrams, this could correspond to an environment similar to a low-coordinated oxide such as NbO_2 [46], which is also in agreement with earlier observations [51]. This could also be an oxynitride as it was detected only at N concentrations of 23 at.% N and above, and was detected in higher intensities in the surface than the bulk, where the most oxidised species typically reside.

In the 37 at.% N samples, components *a*, *c* and *d* as well as an additional *b* component are needed, but their relative binding energy distances are different compared to the 23 at.% N sample. The *d*-*a* core level shift in the 37 at.% N sample is further reduced to 4.4 eV and the *c*-*a* shift is 2.9 eV, *i.e.*, component *c* and *d* are both closer to component *a* in this sample. This may instead be understood as an upward shift of component *a*, as it is affected by the presence of nitrogen. Component *a* could therefore be partially nitrided, even though it is still denoted metal in Fig. 3. Component *b*, with a *b*-*a* chemical shift of +0.9 eV, could be modelled with both asymmetric and symmetric line shapes, where the former would better model the higher conductivity of a nitride and the latter would better model an oxide. The variation of line shape did not alter the result of the fit but it was clear that *b* was constant in intensity relative to the metallic component *a*, and is therefore found at a similar depth to the metal in the sample, motivating the assignment of component *b* as nitride-like Nb.

For the 49 at.% N sample three spin–orbit split components are needed to describe the spectra. The two other components, *c* and *d*, are shifted 1.0 eV and 3.0 eV respectively above the nitride-like component and was earlier assigned to $NbN_{1-y}O_y$ and Nb_2O_5 [52]. Both *c* and *d* increase in intensity relative the nitride signal at lower photon energies, indicating that the oxidised Nb is found on the sample surface.

The Nb 3d spectra for the films with increasing N content show a gradual progression from Nb being metallic (0 and 13 at.% N), to having some interaction with nitrogen (23 at.% N), to the formation of nitride-like Nb (37 and 49 at.% N). An important feature is that only one oxide is formed for the 0 and 13 at.% N films. At higher N concentrations such as 23 at.% and above, two oxidised components, *c* and *d* were seen. Component *d* has a similar binding energy of the Nb $3d_{5/2}$ level of 207.4 ± 0.2 eV for all samples indicating a similar type of oxide. The oxidised component at lower binding energy, component *c*, however shifts towards lower binding energy for the highest nitrogen content, indicating that this is an oxynitrides with varying oxygen/nitrogen ratios.

3.1.4. Y 3d

As shown in Fig. 4, the Y 3d core level spectrum of the 0 at.% N sample was modelled with two spin–orbit split components spaced 2.1 eV apart. Component *a* with a Y $3d_{5/2}$ binding energy of 155.7 ± 0.2 eV, was assigned to metallic Y. Component *c* was assigned to oxidised Y with an oxidation state of 3+. A similar metal-oxide shift has earlier been assigned to Y^{3+} hydroxide [53], but since an hydroxide contribution to the O 1s spectrum is nearly absent (see Supplementary Information Figure S3), we suggest that yttrium is found in an environment more similar to Y_2O_3, which also agrees with Pourbaix diagrams. The components *a* and *c* were found in all the other samples as well (N = 13 – 49 at.%), and the chemical shift between them was 2.2 ± 0.2 eV. However, all the N containing films also required

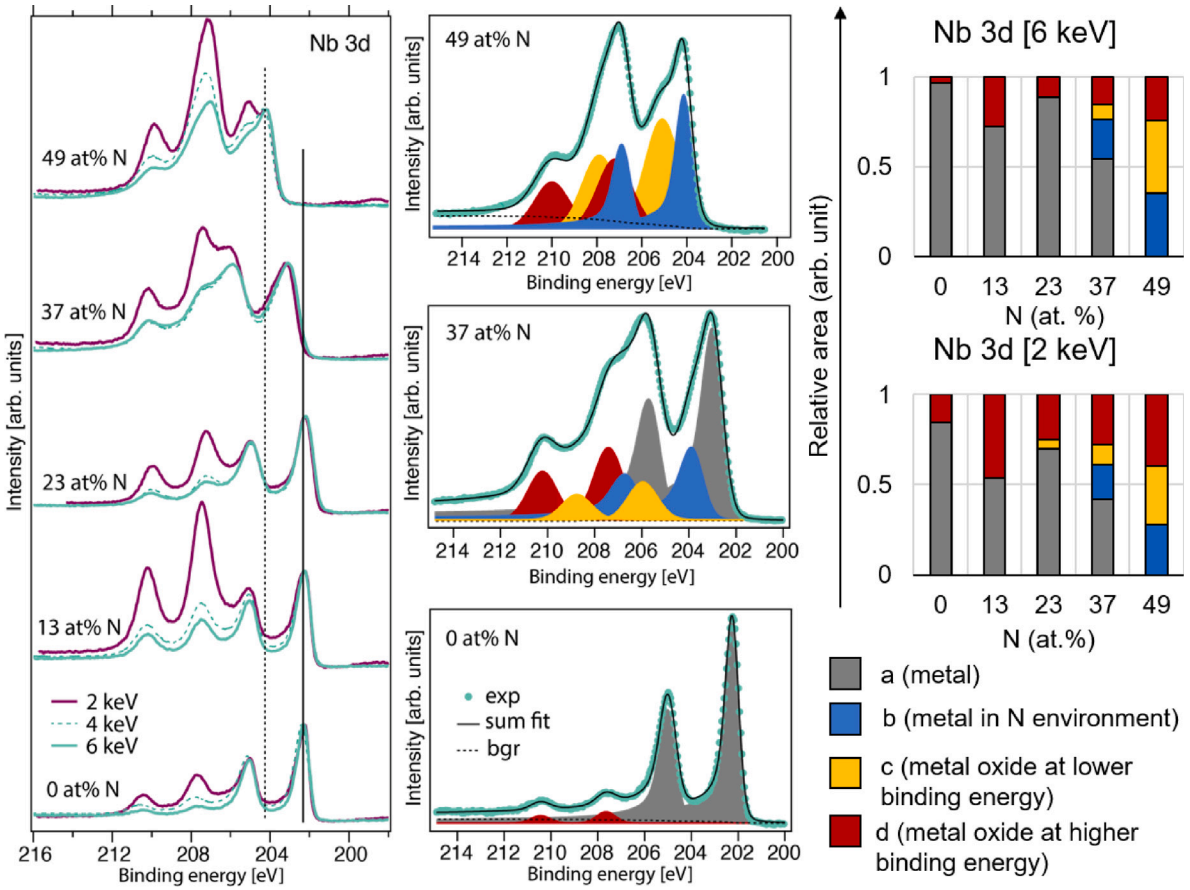

Fig. 3. Nb 3d spectra collected using photon energies of 2, 4 and 6 keV. The left hand side shows the overlaid spectra for all as-deposited $AlCrNbYZrN_x$ samples at all energies, with the intensities normalised to the lowest binding energy peak. Solid (dotted) vertical line indicate position of metal (nitride) components. The centre panel shows the curve fits of the 0, 37 and 49 at.% N samples measured with a photon energy of 6 keV. The shaded areas from the curve fits have been used to create the bar charts on the right where the metal, or partially nitride-like peak is in grey, the nitride-like is in blue and the oxides are in yellow and red.

a third spin–orbit doublet, component *b*, with a *b*-*a* chemical shift of +0.5 ± 0.2 eV. The intensity of component *b* was observed to increase with N content, and was hence assigned to yttrium in a nitride-like or oxynitride environment. This is also in agreement with the metal-nitride shift of 0.4 eV earlier observed [54]. However, the metallic component *a* was also found in all samples, implying that Y was only partially nitrided even when the N content approached 50 at.%. The surface sensitive measurements performed at 2 keV of the 37 at.% N film show a higher proportion of component *b* compared to the bulk sensitive measurements, indicating that an oxidised nitride-like Y was present closer to the surface.

A contribution from a metallic Y component was present in all samples regardless of N content, implying that Y was only partially nitrided. This was in stark contrast to the Al, Cr, Nb, and Zr core level spectra, which showed that there was no metal at the highest N concentration of 49 at.%.

3.1.5. Zr 3d

The Zr 3d core level spectrum of the 0 at.% N sample (shown in Fig. 5) required two spin–orbit split components, labelled *a* and *d*. The asymmetric component *a*, with a Zr $3d_{5/2}$ binding energy of 178.5 ± 0.2 eV, is attributed to metallic Zr. Shifted 4.15 eV towards higher energy, is the symmetric component *d*, assigned to Zr in an oxide environment [52,55]. Several studies and Pourbaix diagrams of Zr indicate that the most stable oxide is ZrO_2 [46]. These metal (*a*) and oxide (*d*) components with the same binding energy shift are also clearly visible in the 13 at.% N sample.

For the 23 at.% N sample, a smaller core level shift of 3.9 eV suggests that the film is affected by the higher N content. Similarly to Nb, component *a* is no longer purely metallic. Two additional spin–orbit components are required: an asymmetric component *b* shifted 1 eV above *a* and an additional symmetric component *c* shifted 2.1 eV above *a*. Component *b* is assigned to nitride-like Zr. Component *c* is probably a low coordination oxide or oxynitride, as it is only seen with N contents of 23 at.% and above, and is present in higher quantities in the surface sensitive measurements close to the high binding energy oxide.

All four components *a*-*d* described above are also found in the 37 at.% N sample. The relative intensity of component *a* is reduced to a shoulder on the low binding energy side in the core level spectra. The nitride-like component *b* is on the other hand more intense compared to the 23 at.% N sample. The shifts for the 37 at.% N film are smaller compared to the 23 at.% N sample: +1.4 ± 0.3 eV for *b*-*a*, +2.0 eV for *c*-*a*, and +3.4 eV for *d*-*a*. Again, this indicates that component *a* is not purely metal-like. Component *c*, assigned to be oxynitride, is found 1.2 above the nitride component *b* for both 23 and 37 at.% N films.

The Zr 3d core level spectra of the 49 at.% N sample was fitted with the three components *b*, *c* and *d*. There was no contribution from component *a* corresponding to metallic Zr. As for the other samples, *b* is assigned to nitride-like Zr, and *c* and *d* to oxynitride and oxide-like Zr, where the *c*-*b* shift was +1.4 ± 0.3 eV and the *d*-*b* shift was +2.1 eV. Component *c* was assigned as an oxynitride as it only appears at N concentrations above 23 at.% and has a higher binding energy than the pure nitride. [56]. We note that component *d* overlaps with the satellite of ZrN [52] but as this component increases relative the main nitride component in more surface sensitive measurements, part of this signal must be from a surface oxide.

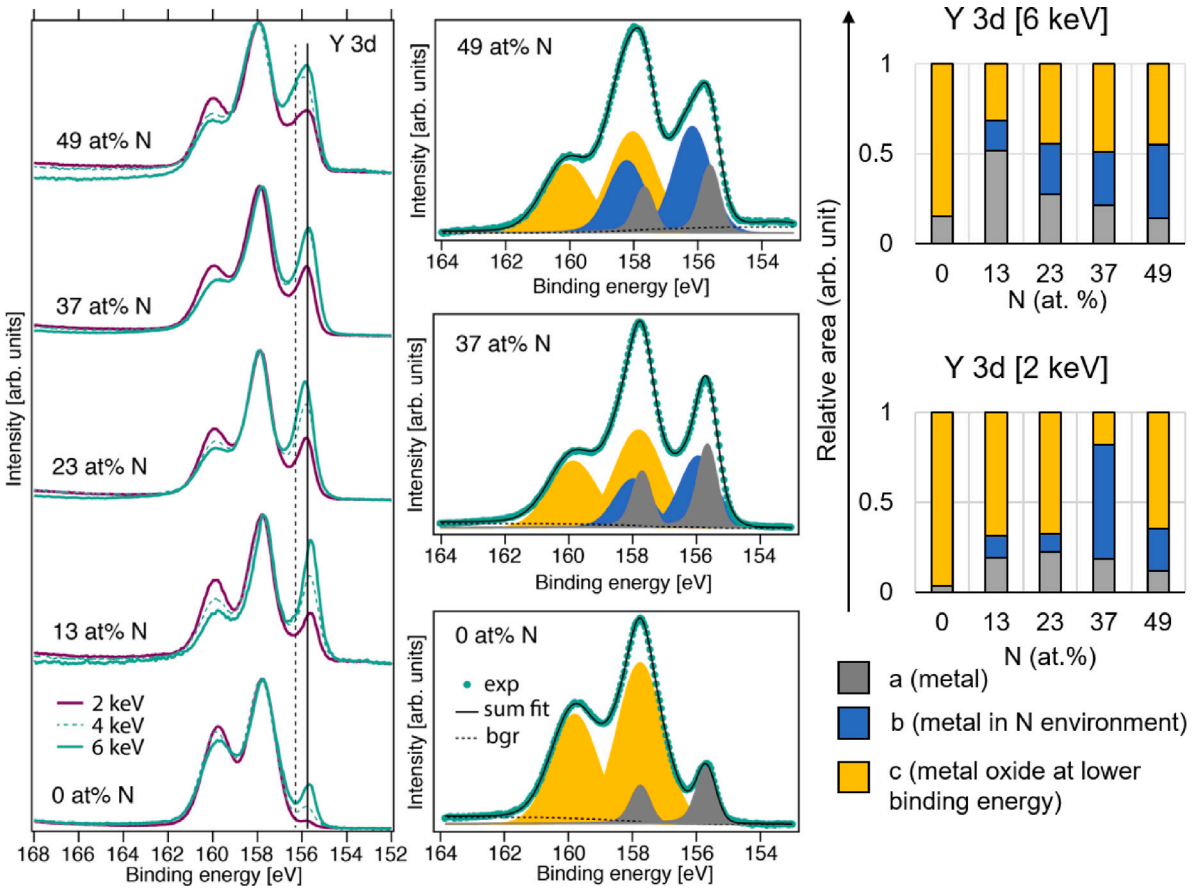

Fig. 4. Y 3d spectra collected using photon energies of 2, 4 and 6 keV. The left hand side shows the overlaid spectra for all as-deposited $AlCrNbYZrN_x$ samples at all energies, with the intensities normalised to the oxide component. Solid (dotted) vertical line indicate position of metal (nitride) components. The centre panel shows the curve fits of the 0, 37 and 49 at.% N samples measured with a photon energy of 6 keV. The shaded areas from the curve fits have been used to create the bar charts on the right where the metal is shown in grey, the nitride-like or oxynitride in blue and the metal oxide in yellow.

3.1.6. *Summary of HAXPES studies of pristine $AlCrNbYZrN_x$ films*

The results of all the curve fits for the metal core level spectra of the as-deposited $AlCrNbYZrN_x$ show the varying oxidation and nitridation behaviour of the individual metals.

A preferential order in which nitrogen interacted with the different metals was observed. At a nitrogen concentration of 13 at.%, the only metal affected by nitrogen was Y. At N = 23 at.%, nitrogen also interacted with Zr and Nb. At N =37 at.% Y, Zr, Al and Nb all showed nitride-like environments, whereas nitride-like Cr was only found at N = 49 at.%. The only element that remained partly metallic at all concentrations was Y. While the order of metal-nitride interaction aligns with the calculated enthalpies of formation of the binary nitrides [57–59] shown in Table S4 in the Supplementary information, the incomplete nitridation of Y to YN was not fully understood. YN and ZrN have the lowest formation enthalpies (*i.e.* most favourable), followed by AlN, NbN and CrN, suggesting that the nitridation of Y should have been rapid and complete.

The results of this HAXPES study mostly agree well with previous studies conducted by von Fieandt et al.[21], except in two respects. Firstly, von Fieandt et al. found that only partial nitridation was achieved for Al and Cr, even at N concentrations of 51 at.%, whereas Figs. 1 and 2 show no signs of metallic Al and Cr at 49 at.% N. Second, von Fieandt et al. observed that Y was not in a nitrided state at any concentration of N, whereas Fig. 4 shows that Y was clearly found in both a nitride or oxynitride-like environment as well as a metallic environment at all the studied N concentrations. The possible reason for the discrepancies could be that sputter etching was performed in the studies by von Fieandt et al. which may preferentially sputter away light elements such as nitrogen. This reveals the utility of using HAXPES for studying the bulk of multicomponent materials.

As revealed by the surface sensitive measurements, the native oxide is complex and contains oxidised species of all the metals. The most oxidised metal oxide is generally found at the outermost surface and has chemical environments similar to Al_2O_3, Cr_2O_3, Nb_2O_5, Y_2O_3 and ZrO_2. Cr, Nb and Zr also show a low-coordinated oxide below the outermost surface with chemical environments similar to CrO, Nb_2O_3 and ZrO. If the process of the formation of the native oxide were to be conceptualised, the low-coordinated oxide may be seen as an intermediate stage that is oxidised further to the most stable oxide. For the higher nitrogen concentrations there are indications that for Nb and Zr this low-coordinated intermediate oxide is in fact an oxynitride. For Al and Y, there are on the other hand indications that the nitride-like component may be an oxynitride.

3.2. *Corroded $AlCrNbYZrN_x$ films*

We have earlier shown, by combining electrochemistry with scanning electron microscopy, that the corrosion resistance of $AlCrNbYZrN_x$ is clearly linked to the microstructure [23], which in turn is dependent on the nitrogen content, see Table 1. A low nitrogen content (0 and 13 at.%) gives porous films with low corrosion resistance. Intermediate nitrogen content (23 and 37 at.%) gives denser films with higher corrosion resistance, while the highest nitrogen content (49 at.%) gives again a porous film with lower corrosion resistance. Despite the varying porosities, all the films had an average surface roughness below 2 nm, as determined using AFM and shown in the Supplementary Information, Figure S8. As there is no correlation between surface roughness

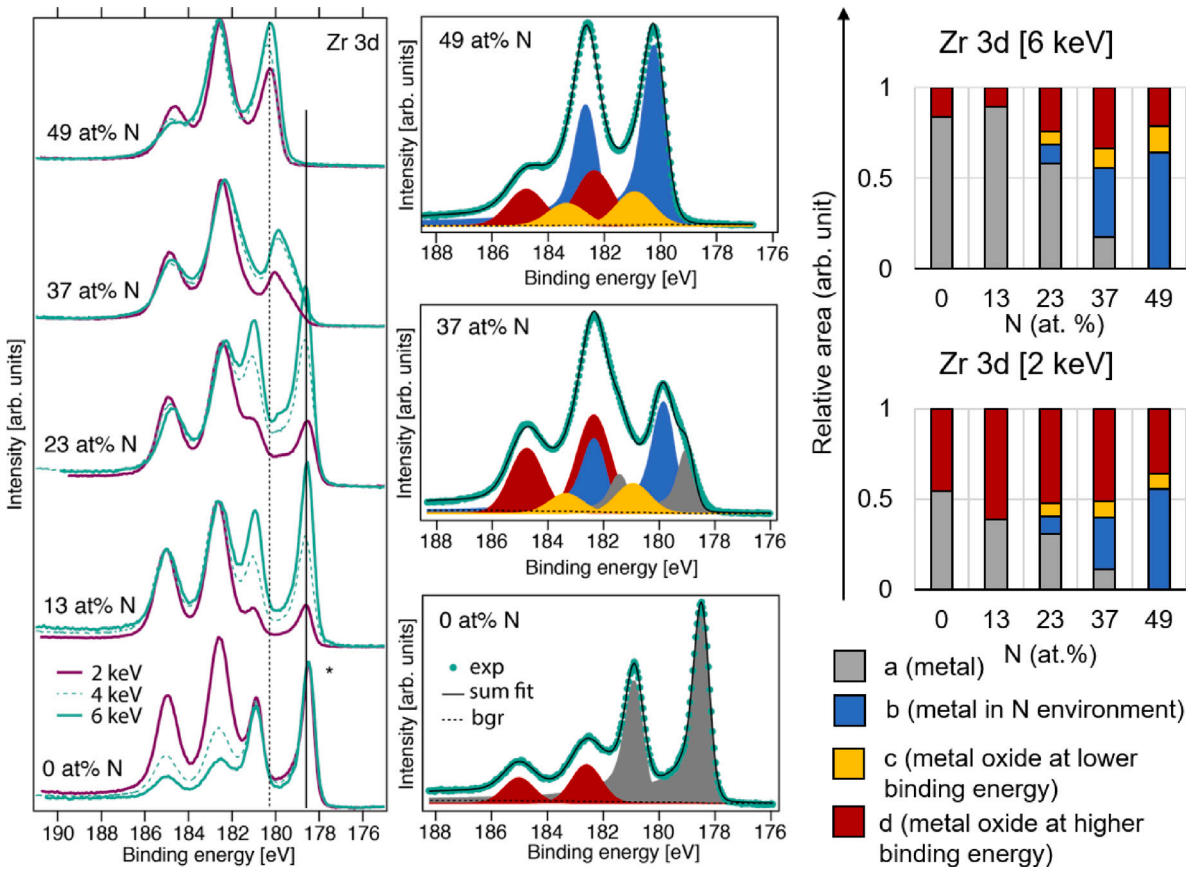

Fig. 5. Zr 3d spectra collected using photon energies of 2, 4 and 6 keV. The left hand side shows the overlaid spectra for all as-deposited $AlCrNbYZrN_x$ samples at all energies. The intensities are normalised to the oxide component, except for the 0 at.%N sample where the asterisk indicates a different intensity scaling *i.e.* in this case the intensities are normalised to the metal peak. Solid (dotted) vertical line indicate position of metal (nitride) components. The centre panel shows the curve fits of the 0, 37 and 49 at.% N samples measured with a photon energy of 6 keV. The shaded areas from the curve fits have been used to create the bar charts on the right where the metal, or partially nitride peak is in grey, the nitride-like is in blue and the oxides are in yellow and red.

and microstructure and as all the films in this study are very smooth, the observed differences in corrosion behaviour appears to be linked to the variation in microstructure rather than the surface roughness.

As discussed above, the pristine multicomponent $AlCrNbYZrN_x$ films showed a layer of several metal oxides and oxynitrides on top of metal nitrides and/or pure metals. Changes in the surface composition were investigated by corroding the $AlCrNbYZrN_x$ films and then performing HAXPES measurements using different photon energies. The films were exposed to 1.0 M HCl for 2 h and then linearly polarised at a rate of 1 mV/s from − 0.7 V to + 0.6 V vs. Ag/AgCl (3 M KCl). The application of the anodic potential provides a driving force for surface oxidation. This would encourage diffusion and oxidation underneath the passive layer to support the changes at the metal-solution interface. The changes in the different proportions of components were acquired from the curve fits for Al 1s, Cr 2p, Nb 3d, Y 3d and Zr 3d core level spectra. The results are shown in Fig. 6 and example spectra comparing pristine and corroded samples can be found in Supplementary Information Figures S5 and S6.

The 0 and 13 at.% N samples were completely etched away during the polarisation, which is due to their high porosity resulting in a homogeneous etching [23]. They were not studied further. The 23, 37, and 49 at.% N films appeared intact after the polarisation. The 49 at.% N film also featured a porous morphology and it is not understood why the 49 at.% N film was not completely lost during the polarisation. HAXPES results in the following section show that the porosity of the 49 at.% N film made it challenging to decipher changes before and after corrosion as the oxide was detected at every depth in the pores, thus producing inconclusive data regardless of photon energy.

3.2.1. Al 1s

A comparison between the samples before and after corrosion show a slight increase in intensity in the lowest binding energy component (*i.e.*, the metal for the 23 and 37 at.% N films and the nitride for the 49 at.% N film). Correspondingly, the components with higher oxidation states, such as the oxide, were lost in the corrosion process. As discussed above, the nitride-like component *b* can be associated with an oxynitride for the 37 at.% N sample. In Fig. 6 this component is seen to decrease after corrosion, indicating it was converted to the oxide.

3.2.2. Cr 2p

The 23 at.% N sample shows a large change in the relative proportions of the different components after corrosion. Both the metallic and low-coordinated oxide decreased in significant amounts, accompanied by an increase in the oxide with high binding energy. This shows a clear progression in oxidation from the metal to the metal oxide of low binding energy to the oxide with higher binding energy. The same trend is seen for the 37 at.% N film. Negligible changes were noted for the 49 at.% N film before and after corrosion. This can be related to the porosity of this sample, which will be discussed further below.

3.2.3. Nb 3d

The trends for Nb are very similar to those of Cr. The 23 at.% N film shows a large increase in the most oxidised *d* component after corrosion. Again this shows a clear progression from the metal to the low binding energy oxide (being either a low-coordinated oxide or an oxynitride) to the most oxidised state of Nb. In the 37 at.% N film there is a similar but less pronounced increase in the *d* component. In the 49 at.% N film there is almost no change at all in the relative proportion of the different components, which is attributed to its porosity.

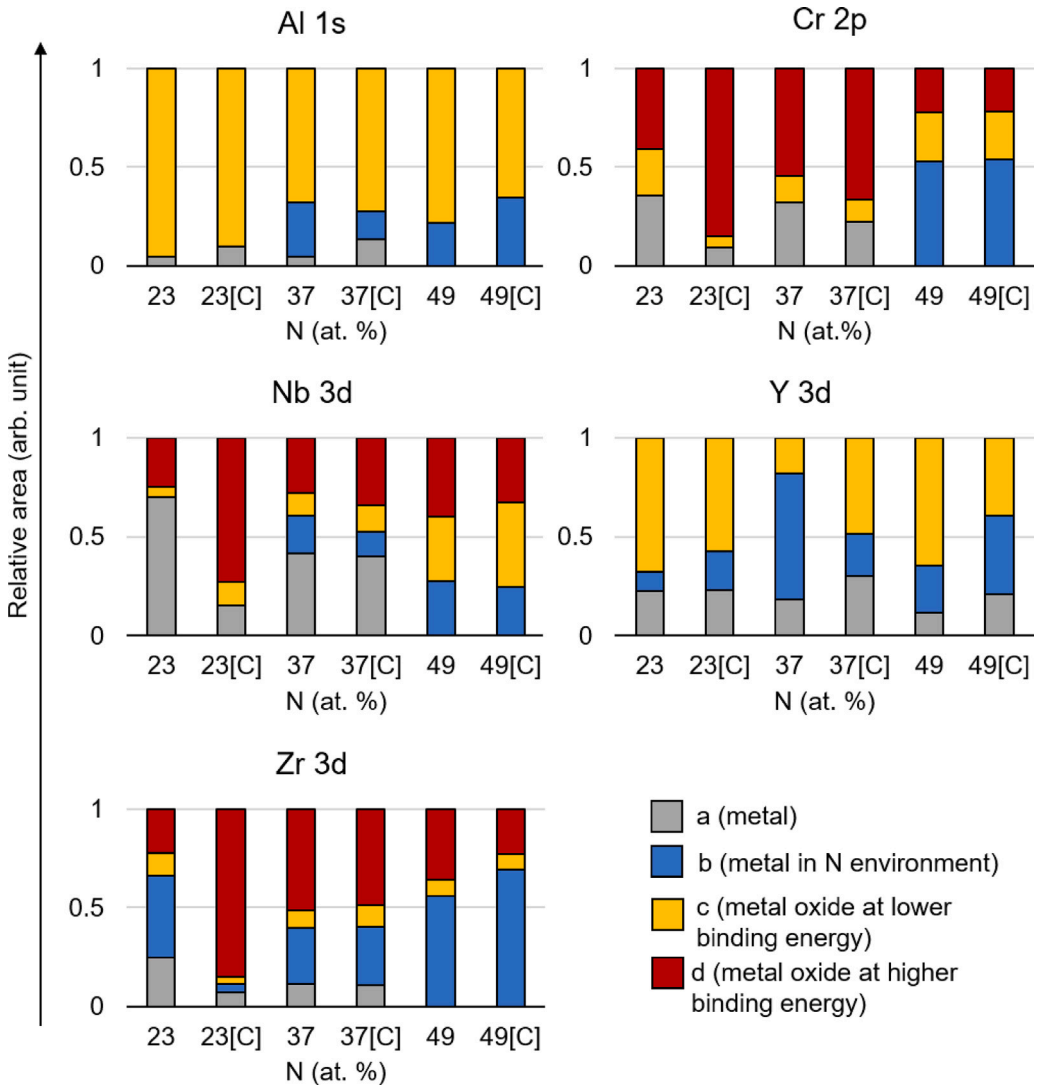

Fig. 6. Comparative contributions from each component of the as-deposited and corroded samples with 23, 37 and 49 at.% N collected at 2 keV. The [C] indicates that the sample was corroded. The data for the as-deposited samples are the same as shown in Figs. 1–5, but shown here again for easy comparison to the corroded samples. The metal contribution is in grey, the nitride-like is in blue, the metal oxide at lower binding energy is in yellow and the metal oxide at higher binding energy is in red (see text for proper assignments).

3.2.4. Y 3d

The metal (*a*), nitride/oxynitride-like (*b*) and oxide (*c*) components are present in all samples both before and after corrosion. After corrosion, the proportion of oxidised yttrium, component *c*, is slightly reduced for the 23 and 49 at.% N samples, indicating that it was lost to the solution. The pristine 37 at.% N sample follows a different trend and appears to have a much lower amount of the oxide and more of nitride/oxynitride-like Y. The reason for this is not understood. However, after corrosion of the 37 at.% N film, there is an increase in the oxidised yttrium, reinforcing the conclusion that the oxynitride was converted to the oxide. After corrosion of the 49 at.% N film, there is a reduction of the oxidised yttrium, thus indicating that it was lost to the solution. The changes in the different components of Y before and after corrosion are however modest.

Pourbaix diagrams indicate that yttrium prefers to exist as Y^{3+} in pH 0 environments and should therefore dissolve in 1.0 M HCl. However, the results in this study as well as in a previous study on the corrosion performance of $AlCrNbYZrN_x$ alloys [23], indicate that yttrium is still present in the passive film after corrosion. A probable explanation for this could be that the dissolution of yttrium is hindered by the overlaying oxides of the other metals such as Cr and Nb, demonstrating the benefits of multicomponent alloying strategies.

3.2.5. Zr 3d

Zirconium is present in the films as metal, nitride-like, oxynitride and oxidised zirconium. After corrosion of the 23 at.% N film in 1.0 M HCl, there is a dramatic increase in component *d*, corresponding to the oxide with the highest oxidation state (zirconium is predominantly quadrivalent in its oxides [46]). For the films with higher N content, the changes were less apparent in the relative abundances between the different components before and after corrosion. For the 37 at.% N film this cannot be attributed to porosity effects as the film was dense. Pourbaix diagrams of Zr would indicate that any Zr oxides should dissolve in pH 0, and it is not known why the 37 at.% N film did not show any apparent changes. An enrichment of the passive layer similar to the 23 at.% N film was expected, but as there were no major losses in Zr in the 37 at.% N film, its dissolution may have been hindered by the presence of Nb and Cr oxides, which are less soluble in 1.0 M HCl. The 49 at.% N film showed a mild loss in Zr oxides.

3.2.6. Summary of HAXPES studies of corroded $AlCrNbYZrN_x$

The results from the measurements using a photon energy of 2 keV presented above show that the passive film changes during corrosion for the 23 at.% N and 37 at.% N films. For Cr, Nb, and to some extent

also Al, the data shows that low-coordinated oxides or oxynitrides are converted to oxides with higher binding energy during corrosion.

If the outermost oxide was largely insoluble (Cr and Nb oxides), then changes in the concentrations of the intermediate suboxide or oxynitride were also correspondingly small. If the oxide had a high solubility in the acid, then changes in the concentration of the intermediate oxynitride were also observed to be larger, as in the case of Al and Y. The HAXPES data thus suggests that the formation and subsequent consumption of the subsurface intermediary suboxides or oxynitrides was correlated to the dissolution of the outermost oxide.

For Zr, the behaviour was different for the different samples, making it difficult to identify any relationships between oxidation and dissolution. The film with a nitrogen concentration of 49 at.% appeared similar before and after corrosion.

A comparison to more bulk sensitive measurements of the corroded films (see Figure S7 in Supplementary Information), shows that the highest amount of oxidised species is clearly found at the outermost surface for the 23 at.% N film. This is also the case, but with smaller changes, for the 37 at.% N film. In contrast, the 49 at.% N film showed no major differences in the intensities of oxidised components irrespective of the photon energy used and therefore regardless of the probing depth. This indicates that the oxide was found all along the porous microstructure in this film.

It is worth noting that, according to their Pourbaix diagrams, some of the metal oxides that were expected to dissolve completely in 1.0 M HCl were still present after the corrosion (as for Y and Zr), indicating a protection from other metal oxides (such as Cr and Nb). The existence of this protective effect is further supported by the absence of drastic changes to the relative surface abundances of the different elements before and after corrosion by potentiodynamic polarisation, as shown by overview spectra in Figure S2 in Supplementary Information. This is different to our earlier study on the same material system where we observed that the surfaces of the densest films were enriched in Cr after 72 h in 1.0 M HCl [23], indicating a dependence on the timescale for corrosion.

4. Conclusion

The surfaces of $AlCrNbYZrN_x$ thin films with nitrogen concentrations ranging from 0 to 49 at.% were studied by HAXPES.

The first metal to interact with nitrogen was Y (at 13 at.% N), followed by Nb and Zr (both at 23 at.% N), Al (at 37 at.% N), and finally Cr (at 49 at.% N). Unlike the other metals, Y remained partly metallic at even at the highest N concentrations. The calculated formation enthalpies of the respective binary nitrides indicated that YN was the most favourably formed. While all five metals obeyed the expected thermodynamic order, the reason behind the partial nitriding of Y was unclear.

The native oxide contained oxidised species of all the metals, with the highest coordination oxides found on the outermost surface. Cr, Nb, and Zr also showed an additional low-coordinated oxide beneath the outermost surface. Indications of oxynitride-like species were also detected for all the elements at high N concentrations of 37 at.% and above correlated to their individual metal–nitrogen enthalpies.

The passive film composition was significantly altered during corrosion in 1.0 M HCl for the 23 at.% N and 37 at.% N films. For Cr, Nb, and Al, the low-coordinated oxides or oxynitrides were converted to the most thermodynamically stable oxides. For Cr and Nb this resulted in an increased amount of the highest oxidised species, whose oxides are known to be stable in the tested conditions [46]. Highly oxidised Al and Y were, on the other hand, lost from the surface during corrosion, in agreement with their lower electrochemical stabilities in 1.0 M HCl.

The oxidation and dissolution behaviour of Zr was irregular for the different samples. At an N concentration of 23 at.% N, it behaved like Al and Y, with a high rate of surface oxidation. However, at N contents of 37 at.% N and above, it behaved like Cr and Nb, showing only minor changes in oxidation and dissolution.

The film with a nitrogen concentration of 49 at.% appeared similar before and after corrosion and also at different depths in the film. This is due to its high porosity where oxides were found within the pores even at larger probing depths, making it difficult to differentiate between the surface and bulk.

CRediT authorship contribution statement

Aishwarya Srinath: Writing – original draft, Investigation, Formal analysis, Data curation. **Kristina von Fieandt:** Validation, Methodology, Investigation, Data curation. **Stefan Fritze:** Investigation, Data curation. **Leif Nyholm:** Writing – review & editing, Supervision. **Erik Lewin:** Writing – review & editing, Supervision, Conceptualization. **Rebecka Lindblad:** Writing – review & editing, Supervision, Project administration, Methodology, Investigation, Formal analysis, Data curation, Conceptualization.

Declaration of competing interest

The authors declare that they have no known competing financial interests or personal relationships that could have appeared to influence the work reported in this paper.

Data availability

Data will be made available on request.

Acknowledgements

This work was carried out with the support of the Diamond Light Source, beamline I09, United Kingdom (proposal SI20537) and we thank Tien-Lin Lee and Pardeep Kumar for excellent support during the beamtime. The research leading to this result has been supported by the project CALIPSOplus under the Grant Agreement 730872 from the EU Framework Programme for Research and Innovation HORIZON 2020.

Appendix A. Supplementary data

Supplementary material related to this article can be found online at https://doi.org/10.1016/j.apsusc.2024.160349.

References

[1] J.-W. Yeh, S.-K. Chen, S.-J. Lin, J.-Y. Gan, T.-S. Chin, T.-T. Shun, C.-H. Tsau, S.-Y. Chang, Nanostructured high-entropy alloys with multiple principal elements: Novel alloy design concepts and outcomes, Adv. Eng. Mater. 6 (5) (2004) 299–303, http://dx.doi.org/10.1002/adem.200300567.

[2] B. Cantor, I. Chang, P. Knight, A. Vincent, Microstructural development in equiatomic multicomponent alloys, Mater. Sci. Eng. A 375 (2004) 213–218, http://dx.doi.org/10.1016/j.msea.2003.10.257.

[3] B. Cantor, Multicomponent and high entropy alloys, Entropy 16 (9) (2014) 4749–4768, http://dx.doi.org/10.3390/e16094749.

[4] U. Hecht, L. Gránásy, T. Pusztai, B. Böttger, M. Apel, V. Witusiewicz, L. Ratke, J. De Wilde, L. Froyen, D. Camel, B. Drevet, G. Faivre, S. Fries, B. Legendre, S. Rex, Multiphase solidification in multicomponent alloys, Mater. Sci. Eng. R 46 (1) (2004) 1–49, http://dx.doi.org/10.1016/j.mser.2004.07.002.

[5] B. Shaw, R. Kelly, What is corrosion? Electrochem. Soc. Interface 15 (1) (2006) 24–26, http://dx.doi.org/10.1149/2.f06061if.

[6] J. Han, S. Nešić, Y. Yang, B.N. Brown, Spontaneous passivation observations during scale formation on mild steel in CO_2 brines, Electrochim. Acta 56 (15) (2011) 5396–5404, http://dx.doi.org/10.1016/j.electacta.2011.03.053.

[7] K. Hashimoto, K. Asami, A. Kawashima, H. Habazaki, E. Akiyama, The role of corrosion-resistant alloying elements in passivity, Corros. Sci. 49 (1) (2007) 42–52, http://dx.doi.org/10.1016/j.corsci.2006.05.003.

[8] J. Mølgaard, A discussion of oxidation, oxide thickness and oxide transfer in wear, Wear 40 (3) (1976) 277–291, http://dx.doi.org/10.1016/0043-1648(76)90120-4.

[9] B.R. Strohmeier, An ESCA method for determining the oxide thickness on aluminum alloys, Surf. Interface Anal. 15 (1) (1990) 51–56, http://dx.doi.org/10.1002/sia.740150109.

[10] H. Göhr, J. Schaller, C.-A. Schiller, Impedance studies of the oxide layer on zircaloy after previous oxidation in water vapour at 400C, Electrochim. Acta 38 (14) (1993) 1961–1964, http://dx.doi.org/10.1016/0013-4686(93)80323-R.

[11] A. Beni, N. Ott, M. Pawelkiewicz, M. Wardé, K. Young, B. Bauer, P. Rajput, B. Detlefs, J. Zegenhagen, R. McGrath, M.-G. Barthés-Labrousse, L.P. Jeurgens, P. Schmutz, Hard X-ray Photoelectron Spectroscopy (HAXPES) characterisation of electrochemical passivation oxide layers on Al–Cr–Fe complex metallic alloys (CMAs), Electrochem. Commun. 46 (2014) 13–17, http://dx.doi.org/10.1016/j.elecom.2014.05.024.

[12] M. Fondell, M. Gorgoi, M. Boman, A. Lindblad, A HAXPES study of Sn, SnS, SnO and SnO_2, J. Electron Spectrosc. Relat. Phenom. 195 (2014) 195–199, http://dx.doi.org/10.1016/j.elspec.2014.07.012.

[13] E. Lewin, J. Counsell, J. Patscheider, Spectral artefacts post sputter-etching and how to cope with them – A case study of XPS on nitride-based coatings using monoatomic and cluster ion beams, Appl. Surf. Sci. 442 (2018) 487–500, http://dx.doi.org/10.1016/j.apsusc.2018.02.191.

[14] B. Tonner, G. Harp, Photoelectron microscopy with synchrotron radiation, Rev. Sci. Instrum. 59 (6) (1988) 853–858, http://dx.doi.org/10.1063/1.1139792.

[15] P. Staron, T. Fischer, T. Lippmann, A. Stark, S. Daneshpour, D. Schnubel, E. Uhlmann, R. Gerstenberger, B. Camin, W. Reimers, et al., In situ experiments with synchrotron high-energy X-rays and neutrons, Adv. Eng. Mater. 13 (8) (2011) 658–663, http://dx.doi.org/10.1002/adem.201000297.

[16] J. Bastidas, C. Torres, E. Cano, J. Polo, Influence of molybdenum on passivation of polarised stainless steels in a chloride environment, Corros. Sci. 44 (3) (2002) 625–633, http://dx.doi.org/10.1016/S0010-938X(01)00072-5.

[17] R.W. Staehle, J.J. Royuela, T.L. Raredon, E. Serrate, C.R. Morin, R.V. Farrar, Effect of alloy composition on stress corrosion cracking of Fe-Cr-Ni base alloys, Corrosion 26 (11) (2013) 451–486, http://dx.doi.org/10.5006/0010-9312-26.11.451.

[18] Z. Tang, L. Huang, W. He, P.K. Liaw, Alloying and processing effects on the aqueous corrosion behavior of high-entropy alloys, Entropy 16 (2) (2014) 895–911, http://dx.doi.org/10.3390/e16020895.

[19] A. Hermas, K. Ogura, Effects of alloying additions on the spontaneous passivation of stainless steels containing copper at different temperatures, Electrochim. Acta 41 (10) (1996) 1601–1609, http://dx.doi.org/10.1016/0013-4686(95)00411-4.

[20] E. Lewin, Multi-component and high-entropy nitride coatings–A promising field in need of a novel approach, J. Appl. Phys. 127 (16) (2020) 160901, http://dx.doi.org/10.1063/1.5144154.

[21] K. von Fieandt, L. Riekehr, B. Osinger, S. Fritze, E. Lewin, Influence of n content on structure and mechanical properties of multi-component Al-Cr-Nb-Y-Zr based thin films by reactive magnetron sputtering, Surf. Coat. Technol. 389 (2020) 125614, http://dx.doi.org/10.1016/j.surfcoat.2020.125614.

[22] K. von Fieandt, E.-M. Paschalidou, A. Srinath, P. Soucek, L. Riekehr, L. Nyholm, E. Lewin, Multi-component (Al,Cr,Nb,Y,Zr)N thin films by reactive magnetron sputter deposition for increased hardness and corrosion resistance, Thin Solid Films 693 (2020) 137685, http://dx.doi.org/10.1016/j.tsf.2019.137685.

[23] A. Srinath, K. von Fieandt, R. Lindblad, S. Fritze, M. Korvela, J. Petersson, E. Lewin, L. Nyholm, Influence of the nitrogen content on the corrosion resistances of multicomponent AlCrNbYZrN coatings, Corros. Sci. 188 (2021) 109557, http://dx.doi.org/10.1016/j.corsci.2021.109557.

[24] M. Frerichs, F. Voigts, S. Hollunder, R. Masendorf, A. Esderts, W. Maus-Friedrichs, Corrosion of aluminium components studied with MIES, UPS and XPS, Appl. Surf. Sci. 252 (1) (2005) 108–112, http://dx.doi.org/10.1016/j.apsusc.2005.01.106.

[25] A. Pivkina, A. Streletskii, I. Kolbanev, P. Ul'Yanova, Y. Frolov, P. Butyagin, J. Schoonman, Mechanochemically activated nano-aluminium: Oxidation behaviour, J. Mater. Sci. 39 (16) (2004) 5451–5453, http://dx.doi.org/10.1023/B:JMSC.0000039264.33941.82.

[26] L. Cunha, M. Andritschky, L. Rebouta, K. Pischow, Corrosion of CrN and TiAlN coatings in chloride-containing atmospheres, Surf. Coat. Technol. 116–119 (1999) 1152–1160, http://dx.doi.org/10.1016/S0257-8972(99)00270-4.

[27] J. Jagielski, A. Khanna, J. Kucinski, D. Mishra, P. Racolta, P. Sioshansi, E. Tobin, J. Thereska, V. Uglov, T. Vilaithong, J. Viviente, S.-Z. Yang, A. Zalar, Effect of chromium nitride coating on the corrosion and wear resistance of stainless steel, Appl. Surf. Sci. 156 (1) (2000) 47–64, http://dx.doi.org/10.1016/S0169-4332(99)00350-5.

[28] A. Chourasia, Core level XPS spectra of Cr and N in chromium nitride films, Surf. Sci. Spectra 7 (2) (2000) 150–166, http://dx.doi.org/10.1116/1.1332716.

[29] K. Baba, R. Hatada, K. Udoh, K. Yasuda, Structure and properties of NbN and TaN films prepared by ion beam assisted deposition, Nucl. Instrum. Methods Phys. Res. B 127–128 (1997) 841–845, http://dx.doi.org/10.1016/S0168-583X(97)00018-9.

[30] K. Havey, J. Zabinski, S. Walck, The chemistry, structure, and resulting wear properties of magnetron-sputtered NbN thin films, Thin Solid Films 303 (1) (1997) 238–245, http://dx.doi.org/10.1016/S0040-6090(96)09529-6.

[31] D. Wang, Y. Fu, M. Hu, D. Jiang, X. Gao, Q. Wang, J. Yang, J. Sun, L. Weng, Effect of Nb content on the microstructure and corrosion resistance of the sputtered Cr-Nb-N coatings, J. Alloys Compd. 740 (2018) 510–518, http://dx.doi.org/10.1016/j.jallcom.2018.01.034.

[32] G. Cubillos, M. Bethencourt, J. Olaya, Corrosion resistance of zirconium oxynitride coatings deposited via DC unbalanced magnetron sputtering and spray pyrolysis-nitriding, Appl. Surf. Sci. 327 (2015) 288–295, http://dx.doi.org/10.1016/j.apsusc.2014.11.168.

[33] J. Li, Z. Chen, J. Jing, J. Hou, Effect of yttrium modification on the corrosion behavior of AZ63 magnesium alloy in sodium chloride solution, J. Magnes. Alloys 9 (2) (2021) 613–626, http://dx.doi.org/10.1016/j.jma.2020.02.027.

[34] N.C. Reger, V.K. Balla, M. Das, A.K. Bhargava, Wear and corrosion properties of in-situ grown zirconium nitride layers for implant applications, Surf. Coat. Technol. 334 (2018) 357–364, http://dx.doi.org/10.1016/j.surfcoat.2017.11.064.

[35] A. Alviz-Meza, W. De La Cruz, V. Kafarov, Y. Ostos, D. Pena-Ballesteros, Yttrium oxide evaluation as coating to reduce the corrosion velocity in industrial equipment working under combustion environments. Case study: Ferritic 9Cr-1Mo steel, J. Phys. Conf. Ser. 1386 (1) (2019) 012091, http://dx.doi.org/10.1088/1742-6596/1386/1/012091.

[36] T.-L. Lee, D.A. Duncan, A two-color beamline for electron spectroscopies at diamond light source, Synchrotron Radiat. News 31 (4) (2018) 16–22.

[37] J. Campbell, T. Papp, Widths of the atomic K–N7 levels, At. Data Nucl. Data Tables 77 (1) (2001) 1–56, http://dx.doi.org/10.1006/adnd.2000.0848.

[38] S. Tanuma, C.J. Powell, D.R. Penn, Calculations of electron inelastic mean free paths. V. Data for 14 organic compounds over the 50–2000 eV range, Surf. Interface Anal. 21 (3) (1994) 165–176, http://dx.doi.org/10.1002/sia.740210302.

[39] E. Kukk, G. Snell, J.D. Bozek, W.-T. Cheng, N. Berrah, Vibrational structure and partial rates of resonant auger decay of the N 1 s→ 2 π core excitations in nitric oxide, Phys. Rev. A 63 (6) (2001) 062702.

[40] E. Kukk, K. Ueda, U. Hergenhahn, X.-J. Liu, G. Prümper, H. Yoshida, Y. Tamenori, C. Makochekanwa, T. Tanaka, M. Kitajima, et al., Violation of the Franck-Condon principle due to recoil effects in high energy molecular core-level photoionization, Phys. Rev. Lett. 95 (13) (2005) 133001.

[41] S. Doniach, M. Ŝunjić, Many-electron singularity in X-ray photoemission and X-ray line spectra from metals, J. Phys. C Solid State Phys. 3 (2) (1970) 285, http://dx.doi.org/10.1088/0022-3719/3/2/010.

[42] J.F. Moulder, W.F. Stickle, P.E. Sobol, K.D. Bomben, Handbook of X-Ray Photoelectron Spectroscopy, Physical Electronics, Inc., 1995.

[43] M. Klasson, A. Berndtsson, J. Hedman, R. Nilsson, R. Nyholm, C. Nordling, Electron escape depth in silicon, J. Electron Spectrosc. Relat. Phenom. 3 (6) (1974) 427–434, http://dx.doi.org/10.1016/0368-2048(74)80029-0.

[44] K. Nishizaki, H. Nohira, K. Takahashi, N. Kamakura, Y. Takata, S. Shin, K. Kobayashi, N. Tamura, K. Hikazutani, T. Hattori, Depth profiling of oxynitride film formed on Si(100) by photon energy dependent photoelectron spectroscopy, Appl. Surf. Sci. 216 (1) (2003) 287–290, http://dx.doi.org/10.1016/S0169-4332(03)00389-1.

[45] C. Ronning, H. Feldermann, R. Merk, H. Hofsäss, P. Reinke, J.-U. Thiele, Carbon nitride deposited using energetic species: a review on XPS studies, Phys. Rev. B 58 (4) (1998) 2207, http://dx.doi.org/10.1103/PhysRevB.58.2207.

[46] M. Pourbaix, Atlas of electrochemical equilibria in aqueous solution, NACE 307 (1974).

[47] W. Fredriksson, S. Malmgren, T. Gustafsson, M. Gorgoi, K. Edström, Full depth profile of passive films on 316l stainless steel based on high resolution HAXPES in combination with ARXPS, Appl. Surf. Sci. 258 (15) (2012) 5790–5797, http://dx.doi.org/10.1016/j.apsusc.2012.02.099.

[48] F. Esaka, K. Furuya, H. Shimada, M. Imamura, N. Matsubayashi, H. Sato, A. Nishijima, A. Kawana, H. Ichimura, T. Kikuchi, Comparison of surface oxidation of titanium nitride and chromium nitride films studied by X-ray absorption and photoelectron spectroscopy, J. Vac. Sci. Technol. A Vac. Surf. Films 15 (5) (1997) 2521–2528, http://dx.doi.org/10.1116/1.580764.

[49] Q. Ma, R.A. Rosenberg, et al., Thermal and electron-beam irradiation effects on the surfaces of niobium for RF cavity production, in: Conference proceedings: The 10th Workshop on RF Superconductivity, 2001, pp. 368–372.

[50] A. Darlinski, J. Halbritter, Angle-resolved XPS studies of oxides at NbN, NbC, and Nb surfaces, Surf. Interface Anal. 10 (5) (1987) 223–237, http://dx.doi.org/10.1002/sia.740100502.

[51] C.-O. Olsson, D. Landolt, Atmospheric oxidation of a Nb–Zr alloy studied with XPS, Corros. Sci. 46 (1) (2004) 213–224, http://dx.doi.org/10.1016/S0010-938X(03)00139-2.

[52] G. Greczynski, D. Primetzhofer, J. Lu, L. Hultman, Core-level spectra and binding energies of transition metal nitrides by non-destructive X-ray photoelectron spectroscopy through capping layers, Appl. Surf. Sci. 396 (2017) 347–358, http://dx.doi.org/10.1016/j.apsusc.2016.10.152.

[53] M. Krawczyk, W. Lisowski, M. Pisarek, K. Nikiforow, A. Jablonski, Surface characterization of low-temperature grown yttrium oxide, Appl. Surf. Sci. 437 (2018) 347–356, http://dx.doi.org/10.1016/j.apsusc.2017.12.121.

[54] W. De La Cruz, J. Díaz, L. Mancera, N. Takeuchi, G. Soto, Yttrium nitride thin films grown by reactive laser ablation, J. Phys. Chem. Solids 64 (11) (2003) 2273–2279, http://dx.doi.org/10.1016/S0022-3697(03)00259-2.

[55] L. Kumar, D. Sarma, S. Krummacher, XPS study of the room temperature surface oxidation of zirconium and its binary alloys with tin, chromium and iron, Appl. Surf. Sci. 32 (3) (1988) 309–319, http://dx.doi.org/10.1016/0169-4332(88)90016-5.

[56] I. Milošev, H.-H. Strehblow, B. Navinšek, Comparison of TiN, ZrN and CrN hard nitride coatings: Electrochemical and thermal oxidation, Thin Solid Films 303 (1–2) (1997) 246–254, http://dx.doi.org/10.1016/S0040-6090(97)00069-2.

[57] A.D. Mah, N.L. Gellert, Heats of formation of niobium nitride, tantalum nitride and zirconium nitride from combustion calorimetry, J. Am. Chem. Soc. 78 (14) (1956) 3261–3263.

[58] NIST Chemistry WebBook, SRD 69, 2021, https://webbook.nist.gov/chemistry/. (Accessed 22 November 2021).

[59] E. Zhao, J. Wang, J. Meng, Z. Wu, Structural, mechanical and electronic properties of 4d transition metal mononitrides by first-principles, Comput. Mater. Sci. 47 (4) (2010) 1064–1071, http://dx.doi.org/10.1016/j.commatsci.2009.12.011.